

ELECTROMAGNETIC MODELING OF OUTCOUPLING EFFICIENCY AND LIGHT EMISSION IN NEAR-INFRARED QUANTUM DOT LIGHT EMITTING DEVICES

A. E. Farghal, S. Wageh, and A. A. El-Azm

Faculty of Electronic Engineering
Menoufia University
Menouf 32952, Egypt

Abstract—We report an analytical exciton emission model based on Green function for simulating the radiation characteristics of near-infrared Quantum Dot-light emitting devices (QD-LEDs). In this model the internally emitted light can be classified into the following modes: Substrate, indium tin oxide (ITO)/organic waveguided, surface plasmonic modes, and external emitted mode. We investigate the influence of the thickness of different layers and the distance between the emitting center and the cathode metal on the emitted power distribution among these modes. In addition, we study the angular radiation profile for the externally emitted radiation and substrate waveguided mode in comparison with Lambertian radiation profile. We show the change of the thickness of the different layers, and the positions of the emitting centers are critical to the optical performance of the device. The optimization of optical performance through device geometry increases the outcoupling efficiency more than five times.

1. INTRODUCTION

QD-LEDs are characterized by low manufacturing cost, compatibility with a variety of substrates, pure and saturated emission colors with narrow bandwidth, and their emission wavelength is easily tuned by changing the size of the quantum dots [1].

Infrared light emitting nanocrystals (NCs), particularly in the last decade, are of growing importance because of their very significant, potential application in optical amplifier media for standard silica-based telecommunication fibers, which has transmission loss and

Received 2 July 2010, Accepted 2 August 2010, Scheduled 17 August 2010

Corresponding author: A. E. Farghal (ahmedfarghal7080@gmail.com).

dispersion minima windows around 0.8 μm , 1.3 μm , and 1.55 μm [2]. Other applications for which infrared (IR) active NCs have been proposed to date include: IR luminescence LEDs [3–5], IR detectors [6–9], modulators in the extended telecommunications-wavelength band (1200–1700 nm) [10], photovoltaic [11], IR laser technologies [12, 13], thermoelectrics devices [14], and long-wavelength labeling [15].

Although electroluminescence from near-infrared/infrared NCs has been demonstrated, its efficiency needs to be improved to meet the requirements of commercialization in the near future. To date, the reported external quantum efficiency (EQE) from such hybrid devices are listed in Table 1.

Table 1. Infrared (IR) quantum-dot light emitting diodes EQE efficiencies.

EQE	wavelength	QD used
0.001%	1.3–1.55 μm	PbSe nanocrystals in a monolayer [3]
0.0086%	1–1.6 μm	core only PbS blended with a polymer [5]
0.27%	\sim 1.15 μm	MEH-PPV-PbS and MEH-PPV-InAs [1]
0.5%	1–1.3 μm	core-shell InAs/ZnSe and MEH-PPV polymer blend [4]
1.15%	1.3–1.5 μm	PbS nanocrystals and a layer of pentacene [16]

The electroluminescence EQE (η_{EL}) of QD-LEDs is expressed as the ratio of photons extracted into the viewing direction to electrons injected and can be written in simplified form as [17],

$$\eta_{\text{EL}} = \eta_{\text{int}} \times \eta_{\text{oc}} = \gamma \times \varphi_{\text{PL}} \times \eta_{\text{oc}} \quad (1)$$

where η_{oc} is the light outcoupling efficiency, which depends on the emissive layer refractive index and device geometry (typically \sim 0.2 for planar organic light emitting devices OLEDs [18]), and γ is the probability of carrier capture to form electron-hole pairs (excitons generated per carrier injected), which depends on the carrier injection balance. φ_{PL} is the luminescence efficiency of NCs: Photons generated per exciton captured [1]. The reported luminescence efficiency φ_{PL} of IR-NCs in solution reaches more than 80% [19], while that in solid films drops to 1% range due to aggregated quenching [3, 19, 20]. The usual term representing the singlet/triplet capture ratio in OLEDs does not appear in this equation due to the large spin-orbit coupling in QDs [21]. The external and internal quantum efficiencies are connected by device outcoupling efficiency.

In view of the foregoing, attempts have been made to improve the EQE of IR QD-LEDs [1, 20, 22]. To the best of our knowledge there is no attempt to improve the EQE of IR QD-LEDs by improving light

outcoupling efficiency η_{oc} . In QD-LEDs, the outcoupling efficiency is very low due to the small escape cone angle for emitted light. This low value can be attributed to the difficulty for light to escape from high refractive index NCs (PbSe has a very large optical refractive index ~ 4.6 [23]). The total reflection limits the light emitting area because of the critical angle. This effect is well-known in inorganic semiconductor light emitting diodes (and in OLEDs) where the external outcoupling efficiency is estimated by classical ray optics to be $1/2n^2$ for large refractive index n [24, 25]. The light which fails to be emitted from the QD-LED is waveguided in organic layers and substrate as well as surface plasmon at metallic cathode. Additionally, absorption in the organic layers and electrodes can play a role.

To understand the optical characteristics of a QD-LEDs, it is useful to have an optical model that can calculate the radiated emission as a function of variations in the device design, and since a large fraction of the emitted light does not exit the device, it is helpful to compute the emitted power inside the device.

We determine the distribution of power emitted into different optical modes, angular emission and radiation spectrum, and examine their dependence on the thickness of the constituent layers and the QD emissive layer position using the dyadic Green's function. To the best of our knowledge it is the first time to theoretically model IR QD-LEDs.

This article is organized as follows: the theoretical model and device architecture used in the simulation are given in Section 2. The simulation results and discussion are presented in Section 3. Finally, conclusions are drawn in Section 4.

2. THEORETICAL FORMULATIONS

Let us consider a QD-LED structure that consists of seven layers as follows: glass substrate, ITO electrode, hole transporting layer (HTL), emitting layer (PbSe QD), electron transporting layer (ETL), a bilayer cathode Mg:Ag/Ag, in addition to semi-infinite air layer (first layer) and semi-infinite glass layer with no loss (last layer), as depicted in Figure 1, where ε_j and d_j represent the complex dielectric constant and the thickness of each layer, respectively. The coefficients T_j , R_j and T'_j , R'_j correspond to the upward and downward traveling eigenfunctions, respectively. Although this model is applicable to any multilayer structure, the following derivations are based on nine-layer device. We consider an exciton with random orientation reside in the fifth QD emission layer located at $z = 0$.

The powerful dyadic Green's function (DGF) method is extended

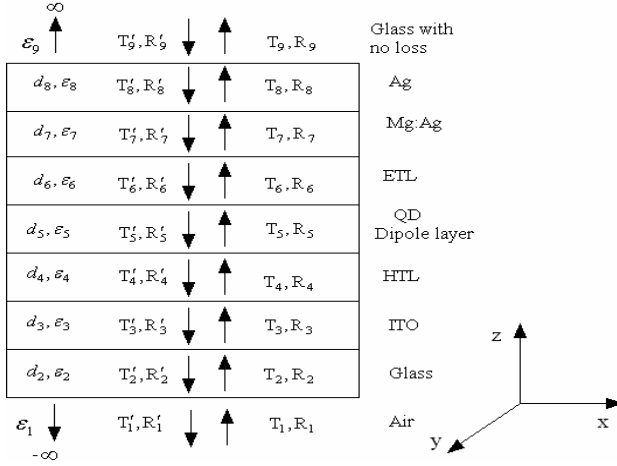


Figure 1. The QDLED multilayer structure used for modeling.

to compute the decay rate of an oscillating exciton in stratified media. We first solve the governing equation for the electric field due to an oscillating current density $J(r)$ [26, 27]

$$\nabla \times \nabla \times E - k^2 E = i\omega\mu_o J(r) \tag{2}$$

where $k = \omega n/c$ is the propagation constant in the region of interest; ω is the oscillation frequency; and n is the complex refractive index. Since the above equation is linear, the dyadic Green formulation for harmonic currents and fields has the standard Green’s function solution (in SI units) [28]:

$$E(r) = i\omega\mu_o \int \bar{G}(r, r') J(r') dV(r') \tag{3}$$

where μ_o is the magnetic permeability; $J(r')$ is the current density; and $\bar{G}(r, r')$ is the DGF which represents the response of a physical system due to a point exciting source. Substituting Equation (3) into Equation (2) yields

$$\nabla \times \nabla \times \bar{G}(r, r') - k^2 \bar{G}(r, r') = \bar{I} \delta(r - r') \tag{4}$$

where \bar{I} is the unit dyadic, and $\delta(r - r')$ is Dirac delta function. Thus for any stratified media, one finds $\bar{G}(r, r')$, and the calculation of the decay rates for any oscillating exciton distribution is straightforward. Let \bar{G}_o denote the Green’s function for the source existing in the emission QD

layer (fifth layer)

$$\bar{G}_o(r, r') = \frac{i}{4\pi} \int_0^\infty dK \sum_{\substack{n=0 \\ t=e,o}}^\infty \frac{2 - \delta_{n0}}{Kh_5} \left[\begin{aligned} &M_{tm\lambda}(h_5, r) M_{tm\lambda}(-h_5, r') \\ &M_{tm\lambda}(-h_5, r) M_{tm\lambda}(h_5, r') \\ &+ N_{tm\lambda}(h_5, r) N_{tm\lambda}(-h_5, r') \\ &+ N_{tm\lambda}(-h_5, r) N_{tm\lambda}(h_5, r') \end{aligned} \right] \begin{aligned} &z \geq 0 \\ &z \leq 0 \end{aligned} \quad (5)$$

where $h_5 = \sqrt{k_5^2 - K^2}$, $k_5^2 = \varepsilon_5(\omega/c)^2$, K and h are the amplitudes of the horizontal and vertical components of the propagation vector, \bar{k} , respectively. M and N , two sets of eigenfunctions, stand for TE and TM modes, respectively [29] and can be written in cylindrical coordinates \hat{r} , $\hat{\phi}$, \hat{z} [27]:

$$\begin{aligned} M_{e_m\lambda}(h, r) &= e^{ihz} \left[\mp \frac{nJ_m(Kr)}{r} \frac{\sin m\varphi\hat{r}}{\cos m\varphi\hat{\phi}} - \frac{\delta J_m(Kr)}{\delta r} \frac{\cos m\varphi\hat{r}}{\sin m\varphi\hat{\phi}} \right] \quad (6) \\ N_{e_m\lambda}(h, r) &= \frac{e^{ihz}}{k_j} \left[ih \frac{\delta J_m(Kr)}{\delta r} \frac{\cos m\varphi\hat{r}}{\sin m\varphi\hat{\phi}} \mp imh \frac{J_m(Kr)}{r} \frac{\sin m\varphi\hat{r}}{\cos m\varphi\hat{\phi}} \right. \\ &\quad \left. + \lambda^2 J_m(Kr) \frac{\cos m\varphi\hat{z}}{\sin m\varphi\hat{\phi}} \right] \quad (7) \end{aligned}$$

where J_m is the first-kind Bessel function, and e and o represent even and odd eigenfunctions, respectively.

The scattered part of the Green function in the nine media \bar{G}_i ($i = 1, 2, 3, \dots, 9$), which corresponds to the contribution of the multiple reflection and transmission waves in the presence of the interfaces, is written as

$$\bar{G}_1(r, r') = \frac{i}{4\pi} \int_0^\infty dK \sum_{\substack{n=0 \\ t=e,o}}^\infty \frac{2 - \delta_{n0}}{Kh_5} [T'_1 M_{tn\lambda}(-h_1, r) M_{tn\lambda}(h_5, r') + R'_1 N_{tn\lambda}(-h_1, r) N_{tn\lambda}(h_5, r')] \quad (8)$$

in the air layer

$$\begin{aligned} \bar{G}_j(r, r') &= \frac{i}{4\pi} \int_0^\infty dK \sum_{\substack{n=0 \\ t=e,o}}^\infty \frac{2 - \delta_{n0}}{Kh_5} [T'_j M_{tn\lambda}(-h_j, r) M_{tn\lambda}(h_5, r') \\ &+ R'_j N_{tn\lambda}(-h_j, r) N_{tn\lambda}(h_5, r') + T_j M_{tn\lambda}(h_j, r) M_{tn\lambda}(h_5, r') \\ &+ R'_j N_{tn\lambda}(h_j, r) N_{tn\lambda}(h_5, r')] \quad (9) \end{aligned}$$

in the j th ($j = 2, 3, 4, 5, 6, 7, 8$) layer

$$\begin{aligned} \bar{G}_9(r, r') = \frac{i}{4\pi} \int_0^\infty dK \sum_{\substack{n=0 \\ t=e,o}}^\infty \frac{2 - \delta_{n0}}{Kh_5} [T_9 M_{tn\lambda}(h_9, r) M_{tn\lambda}(h_5, r') \\ + R_9 N_{tn\lambda}(h_9, r) N_{tn\lambda}(h_5, r')] \end{aligned} \quad (10)$$

in the no-loss glass layer.

where $h_j^- = \sqrt{k_j^2 - K^2}$, $k_j^2 = \varepsilon_j(\omega/c)^2$, and j is the layer index.

The differential Equation (4) alone is insufficient to determine Green's function uniquely, and it is necessary to apply additional conditions. These conditions are (1) the radiation condition at infinity wherever the region extends to infinity and (2) the boundary conditions at interfaces. The absence of $M_{tn\lambda}(h_1, r)$ and $N_{tn\lambda}(h_1, r)$ in $\bar{G}_1(r, r')$ ensures that the field satisfies the radiation condition as $z \rightarrow -\infty$, just as the absence of $M_{tn\lambda}(-h_9, r)$ and $N_{tn\lambda}(-h_9, r)$ in $\bar{G}_9(r, r')$ guarantees that the fields satisfy the radiation condition as $z \rightarrow +\infty$.

The DGF $\bar{G}(r, r')$ satisfies the following boundary conditions across the interfaces between j and $j + 1$ layers (where $j \neq 9$)

$$\hat{e}_z \times \bar{G}_j = \hat{e}_z \times \bar{G}_{j+1} \quad (11a)$$

$$\hat{e}_z \times \nabla \times \bar{G}_j = \hat{e}_z \times \nabla \times \bar{G}_{j+1} \quad (11b)$$

We find

$$T_j e^{-ih_j z_j} + T'_j e^{ih_j z_j} = T_{j+1} e^{-ih_{j+1} z_j} + T'_{j+1} e^{ih_{j+1} z_j} \quad (12)$$

$$\frac{h_j}{k_j} \left(-R_j e^{-ih_j z_j} + R'_j e^{ih_j z_j} \right) = \frac{h_{j+1}}{k_{j+1}} \left(-R_{j+1} e^{-ih_{j+1} z_j} + R'_{j+1} e^{ih_{j+1} z_j} \right) \quad (13)$$

$$h_j \left(-T_j e^{-ih_j z_j} + T'_j e^{ih_j z_j} \right) = h_{j+1} \left(-T_{j+1} e^{-ih_{j+1} z_j} + T'_{j+1} e^{ih_{j+1} z_j} \right) \quad (14)$$

$$k_j \left(R_j e^{-ih_j z_j} + R'_j e^{ih_j z_j} \right) = k_{j+1} \left(R_{j+1} e^{-ih_{j+1} z_j} + R'_{j+1} e^{ih_{j+1} z_j} \right) \quad (15)$$

where z_j is the distance to the j th boundary in the z direction. In the N th (highest) layer $T'_N = R'_N = 0$, so the above equations can be solved for T_{N-1} and T'_{N-1} in terms of T'_N and for R_{N-1} and R'_{N-1} in terms of R'_N . Then the next set is solved for T_{N-2} , T'_{N-2} , R_{N-2} and R'_{N-2} and so on until T_1 , T'_1 , R_1 and R'_1 are known in terms of T_N and R_N . After obtaining these coefficients, the Green's function in all regions can be calculated accordingly.

According to the classical phenomenological approach of CPS, the normalized decay rate of the oscillating exciton can be obtained in terms of the imaginary part (\Im) of the reflected field at the exciton site as:

$$\hat{b} = \frac{b}{b_o} = 1 + \frac{3qn_5^2}{2\mu_o k_5^3} \Im(E_o) \quad (16)$$

where $b_o = \frac{e^2 k_5^3}{6\pi\mu\omega\varepsilon}$ is the natural decay rate in vacuum; E_o is the magnitude of the electric field at the exciton position; e is the electron charge; μ is the reduced mass of the exciton (electron-hole pair); ε is the permittivity; q is the intrinsic quantum yield of the emitting material; n_5 is the refractive index of the medium containing the exciton; and k_5 is the propagation constant ($k_5 = \omega n_5/c$) [26–28]. For oscillating exciton oriented vertical, the normalized decay rate is

$$\hat{b}_V = 1 - q + q \left\{ 1 + \frac{3}{2} \Re \left[\int_0^\infty dK \frac{K^3}{h_5 K_5^3} (R_5 + R'_5) \right] \right\} \quad (17)$$

and for an exciton oriented horizontal, the normalized decay rate is

$$\hat{b}_H = 1 - q + q \left\{ 1 + \frac{3}{4} \Re \left[\int_0^\infty dK \frac{K}{h_5 K_5} \left(T_5 + T'_5 + \frac{h_5^2}{K_5^2} R_5 + R'_5 \right) \right] \right\} \quad (18)$$

We analytically determine the Poynting vector, since the magnitude of \bar{S} has the units of watts per square meter and represents the power flux through a given area, then apply the divergence theorem to convert the volume integral into a surface integral $\int \Delta \cdot S dV = \oint S \cdot dA \approx \int S_z dA$. The real part of \bar{S} represents the real power flux density, so the final form of the Poynting vector in the z direction is given by [27]

$$\Re \left(\int S_{z,j}^V dA \right) = \frac{3q}{4} \Re \left[\int_0^\infty du \frac{u^3 (\sqrt{\varepsilon_j})^*}{|1 - u^2| \sqrt{\varepsilon_j}} \sqrt{(\varepsilon_j/\varepsilon_5 - u^2)} \left(R'_j e^{ih_j z} - R_j e^{-ih_j z} \right) * \left(R'_j e^{ih_j z} + R_j e^{-ih_j z} \right) \right] \quad (19)$$

$$\begin{aligned} \Re \left(\int S_{z,j}^H dA \right) &= \frac{3q}{8} \Re \left[\int_0^\infty du \frac{u (\sqrt{\varepsilon_j})^*}{\sqrt{\varepsilon_j}} \sqrt{(\varepsilon_j/\varepsilon_5 - u^2)} \right. \\ &\quad \left(R'_j e^{ih_j z} - R_j e^{-ih_j z} \right) \left(R'_j e^{ih_j z} + R_j e^{-ih_j z} \right)^* \\ &\quad + \int du \frac{u \left(\sqrt{(\varepsilon_j/\varepsilon_5 - u^2)} \right)^*}{|1 - u^2|} \left(T'_j e^{ih_j z} + T_j e^{-ih_j z} \right) \\ &\quad \left. \left(T'_j e^{ih_j z} - T_j e^{-ih_j z} \right)^* \right] \quad (20) \end{aligned}$$

where $u = \lambda/k_5$ is the normalized parallel wavevector at exciton location. The exciton power transfer efficiency to an individual layer as a unitless percentage of the total power emitted is found by taking

the difference of the magnitude of this flux found at both boundaries of the layer and then dividing it by \hat{b}_v or \hat{b}_H .

In the case of plane waves propagating through multilayers, an emitting angle θ_{air} in the air region is associated with k_{\parallel} and wavevector $k_o = 2\pi n_{air}/\lambda$, according to the formula of $k_o \sin \theta_{air} = k_{\parallel}$. The power in the k_{\parallel} space can be transformed to a power in the real spatial space. The intensity angular distribution is related to the power P by

$$I(\theta_{air}) = \frac{P(k_{\parallel})}{2\pi \tan(\theta_{air})} \quad (21)$$

where $P(k_{\parallel})$ is the power emitted in air as a function of k_{\parallel} .

Each exciton will decay to the ground state and emit a photon with a certain probability. We use $P_r(\lambda)$ to represent the probability of the radiative exciton emitting a photon at wavelength λ . The wavelength of the emitted photon has a distribution that is proportional to the measured photoluminescence (PL) of the emitting material. The distribution can be written as follows [30]:

$$P_r(\lambda) = \frac{I_{PL}(\lambda)}{\sum_{\lambda'} I_{PL}(\lambda')} \quad (22)$$

where $I_{PL}(\lambda)$ is the normalized PL intensity of the emitting material. The electroluminescence (EL) spectrum can be obtained as follows:

$$I_{EL}(\lambda) = \eta_{oc}(\lambda) \cdot P_r(\lambda) \quad (23)$$

where $\eta_{oc}(\lambda)$ is photon out-coupling efficiency at each wavelength.

A basic configuration of bottom-emitting IR QD-LED is selected [3]. The elementary device depicted in Figure 2 corresponds

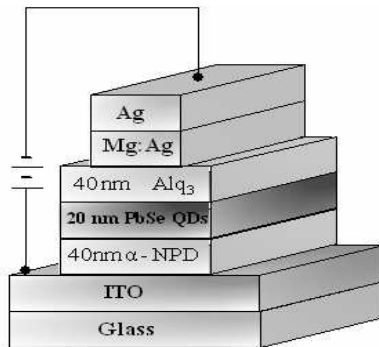


Figure 2. The schematic of the IR QD-LED device structure.

to the structure of Figure 1. The device consists of a glass substrate, (160 nm) ITO anode, (40 nm) 4,4-bis[*N*-(1-naphthyl)-*N*-phenyl-amino]biphenyl (α -NPD) HTL, (20 nm) PbSe QD monolayer as emitting layer radiates typically at 1.55 μm , (40 nm) tris-(8-hydroxyquinoline) aluminum (Alq_3) ETL, and metal cathode (50 nm thick Mg/Ag, by weight, 50 nm Ag cap). Complex refractive indices constants of Alq_3 and α -NPD are taken from [31], and optical constants of PbSe, ITO and Mg:Ag are taken from [32].

3. RESULTS AND DISCUSSION

We investigate how the position of the emitting exciton within the emission QD layer affects on the strength of the coupling to different modes and thus the optical efficiency of the device. We have calculated the distribution of IR emission from QD-LED, which radiates typically at 1.55 μm as a function of the exciton position within the emitting QD layer. Here we consider the QDs packed regularly with center-to-center distance equal to 5 nm, with the exciton located in the QD center.

The distribution of the emitted power into external, substrate waveguided, ITO/organic waveguided and surface plasmon modes as a function of the exciton distance from the cathode is depicted in Figure 3. It is readily observed that the fraction of the power coupled to the ITO layer is largely dependent on the emitting center position within the emitting QD layer and increases with increasing the distance from the metal cathode. When the emitting center is very close

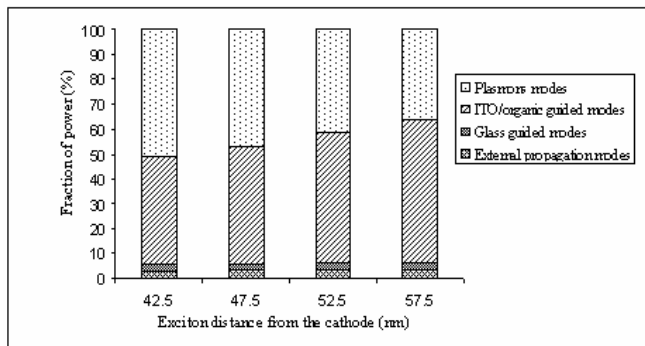


Figure 3. Calculated distribution of the fraction of emission into external, substrate waveguided, ITO/organic modes and surface plasmon waveguided modes as a function of the exciton distance from the cathode.

to the cathode, most of the power is coupled into surface-plasmon modes, which was automatically included in our calculations by using a complex refractive index ($-116.38 + i11.102$) for Ag and ($-171.87 + i256.34$) for Mg electrode at $1.55\ \mu\text{m}$ wavelength. Averaging over the entire emission QD layer we find that the outcoupling efficiency $\eta_{oc} = 3.3287\%$.

This low η_{oc} value can be attributed to the difficulty for light to escape from high refractive index PbSe QD layer. In addition, the optical mode overlap with the emissive QD layer is poor for the long wavelength ($1.55\ \mu\text{m}$). We further note that the choice of ITO as the anode in this devices is not ideal, since the transparency of $150\ \text{nm}$ ITO thickness for the IR electromagnetic wave is only about 70% at $\lambda = 1.5\ \mu\text{m}$ [3].

The low η_{oc} of this device can be optimized by the choice of suitable organic semiconductors materials used in the device, which was originally optimized for visible emitting OLEDs [33]. In this paper, we investigate device optimization through device geometry by varying the thicknesses of the constituent layers.

To verify our model, we compare the emission spectrum with the experimental EL of the same device structure used in our simulations: glass substrate, $160\ \text{nm}$ ITO anode, $40\ \text{nm}$ α -NPD HTL, $20\ \text{nm}$ PbSe quantum dot emitting layer radiates typically at $1.55\ \mu\text{m}$, $40\ \text{nm}$ Alq₃ ETL, and metal cathode ($50\ \text{nm}$ thick Mg/Ag, by weight, $50\ \text{nm}$ Ag cap). The simulation results and experimental data are in a good agreement as shown in Figure 4. So, we can use this model to study the effect of the device geometry on the outcoupling efficiency.

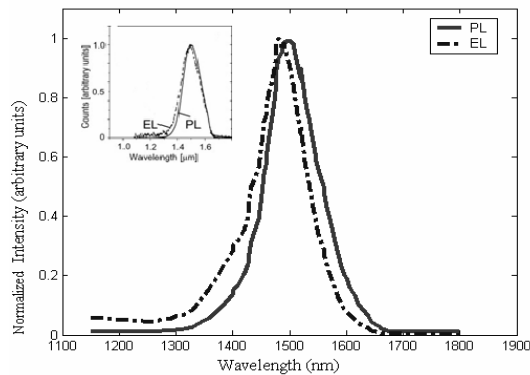


Figure 4. Simulated photoluminescence (PL) and electroluminescence (EL) spectra of the device under study. Inset shows the experimental measurements [3].

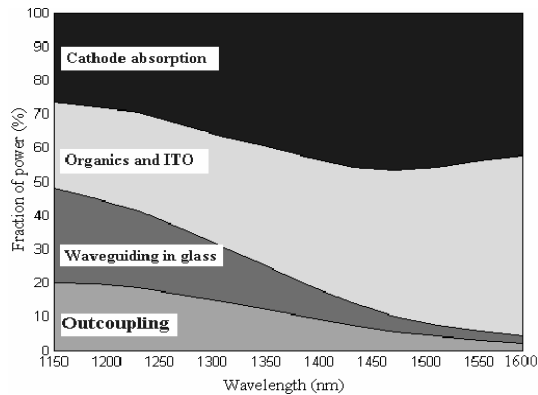


Figure 5. The calculated distribution of PbSe QDs emitted power into the different four optical modes versus the emission wavelength.

The wavelength effect on the fraction of power coupled to each optical mode is shown in Figure 5. We note that the air outcoupling and waveguiding in glass decrease with increasing the emission wavelength in contrast to ITO/organics modes and absorption in the cathode, which increases with increasing the emission wavelength. This variation is attributed to the wavelength dependence on the complex refractive indices of the materials used. It is clear that the materials used are not suitable for IR devices.

We have studied the angular radiation profile for vertically oriented exciton emission and horizontally oriented exciton emission. Figure 6 shows the angular radiation profile of vertically oriented exciton emission. It is clear that most of the radiation from the vertical exciton is emitted above the critical angle (41.8°) and thus cannot escape from the glass substrate into the air. Thus the vertical exciton causes even more waveguiding and surface-plasmon coupling.

Figure 7 shows the angular radiation profile of horizontally oriented exciton emission. The horizontal excitons dominate the radiated emission due to their strength around the normal. Here we observe that there is a much stronger beaming of the light in the forward direction, due to the large refractive index of the emitting QD layer in the IR region relative to the other layers. It is clearly noticed that the radiation profile is not Lambertian which is consistent with the previously reported results for IR QD-LEDs [4, 16].

We have investigated the effect of using different thicknesses for the ETL on the fraction of the fraction of the externally emitted power and the fraction of the emitted power coupled into different optical modes. Figure 8 shows the fraction of the emitted power coupled into

external, substrate waveguided, ITO/organic waveguided and surface plasmon waveguided modes as a function of ETL thickness. Clearly, the fraction of power that is coupled into external and substrate modes is weakly affected by changing the thickness of the ETL. On the other hand, the ITO/organic waveguided and surface plasmon waveguided modes are strongly affected by changing the thickness of the ETL. The change of the thickness of the ETL leads to changing the emission layer

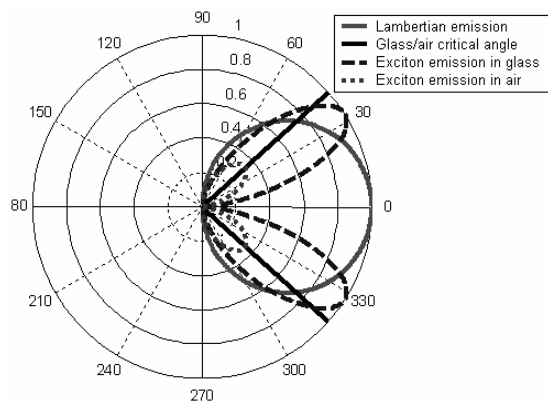


Figure 6. Radiation profiles of the vertical exciton sources of IR-QDLED from. The Lambertian-radiation pattern is also presented for reference.

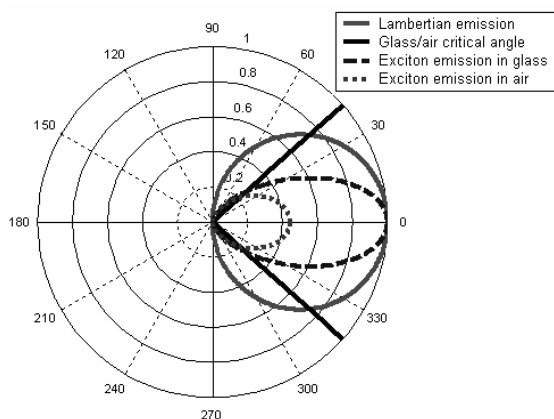


Figure 7. Radiation profiles of the horizontal exciton sources of IR QD-LED. The Lambertian-radiation pattern is also presented for reference.

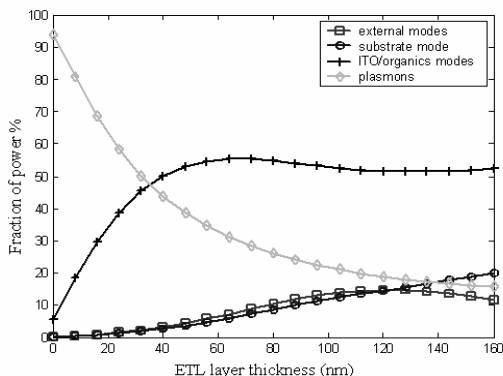


Figure 8. The fraction of the emitted power coupled into external, substrate waveguided, ITO/organic modes and surface plasmon waveguided modes as a function of the ETL (Alq_3) layer thickness variation.

position with respect to the metal cathode, consequently affecting the power coupled to surface plasmon mode. For the external emission mode there is a maximum at ETL thickness ~ 120 nm, which is compatible with the mode overlap with the emissive QD layer for this structure. We have calculated the (η_{oc}) for this maximum of emission and found it 14.8050%.

Figure 9 shows the effect of varying the HTL thickness on the fraction of power coupled to the different four optical modes. In Figure 9, one can see that the HTL layer thickness variation has a little effect on the external emission and substrate waveguided modes. The ITO/organics waveguided and plasmon modes depend greatly on HTL layer thickness. As the HTL layer is located between the emission layer and ITO anode, varying the HTL thickness leads to changing the position of the emitting center relative to ITO anode. ITO behaves as a metal in the IR region; consequently, there will be a great loss of the emitted power into ITO/organics waveguided and surface plasmon modes when the emitting center closes to the ITO anode. Optimization through HTL geometry can be more realized by taking into account the electrical characteristics of the QD-LED (i.e., carrier mobility and the injection efficiency of the anode), which is not covered in this work.

Figure 10 shows the effect of varying ITO layer thickness on the four optical modes. Obviously, the thickness of ITO affects the distribution of power coupled to the four optical modes. It alters the ITO/organic modes by changing the combined thickness of the ITO/organic layer. As we can see from Figure 10 that the direct

emission decreases with increasing thickness of the ITO layer, and the ITO/organic modes is suppressed at very thin ITO thickness. The decrease of ITO thickness causes an increase of sheet resistance of the anode and consequently affects the electrical characteristics of the device. The improvement in the direct emission and reduction of ITO/organic waveguided modes are not significant as that obtained by decreasing ITO thickness in the OLED working in the visible band [34, 35]. This is due to the high transparency of thin ITO in the 400–1000 nm visible region and the high metallic-like reflectivity of ITO in the IR region [36]. So the choice of ITO as the anode in IR QD-LED devices is not ideal [3]. Optimization through using different types of anode will be the subject of further study.

On the other hand, we have calculated the fraction of the emitted power coupled into different optical modes for another two different structures. The first structure is ITO/ α -NPD/Alq₃:QD/Ag. We have investigated the effect of successively moving the position of the emitting center (QD) within the ETL layer on the fraction of the emitted power coupled into different optical modes. Figure 11 shows the fraction of emitted power into external, substrate waveguided, ITO/organic waveguided and surface plasmon waveguided modes. Obviously, the fraction of external emitted light and substrate wave guided modes are strongly decreased when the emitting center is moving closer to the cathode. This is due to strongly increasing plasmonic mode, which gains power on shortening the distance of the emitting center (QD) to the metallic cathode. Conversely, the surface plasmon waveguided modes increases when the emitting center

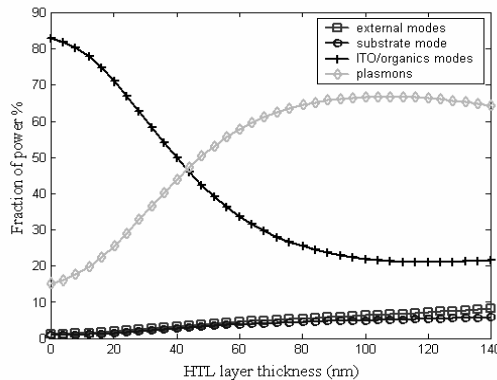


Figure 9. The fraction of the emitted power coupled into external, substrate waveguided, ITO/organic modes and surface plasmon waveguided modes as a function of the HTL layer thickness variation.

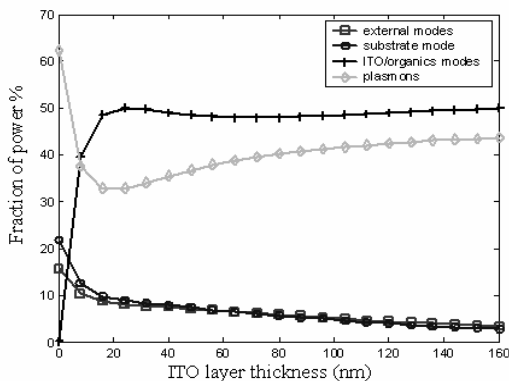


Figure 10. The fraction of the emitted power coupled into external, substrate waveguided, ITO/organic modes and surface plasmon waveguided modes as a function of the ITO layer thickness variation.

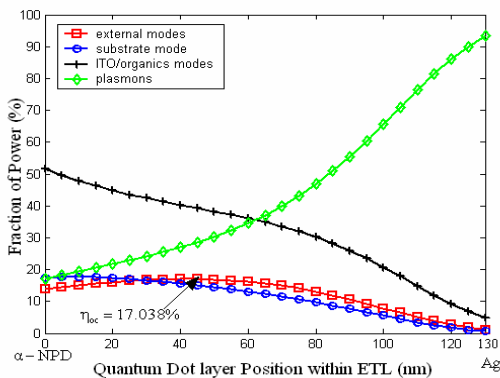


Figure 11. The fraction of the emitted power coupled into external, substrate waveguided, ITO/organic modes and surface plasmon waveguided modes as a function of Quantum dot layer position in the ETL layer.

is moving closer to the cathode and growing to maximum value when the position of the emitting center lies directly beside the cathode metal. On the other hand, when the position of the emitting center moves away from the cathode the η_{oc} increases and has a maximum value 17.0380% at QD located at 45 nm from the Alq₃/α-NPD interface and 85 nm from the Ag cathode, which is nearly five times greater than the value calculated for the original device shown in Figure 2.

The second structure is ITO/α-NPD:QD/Alq₃/Ag. We have

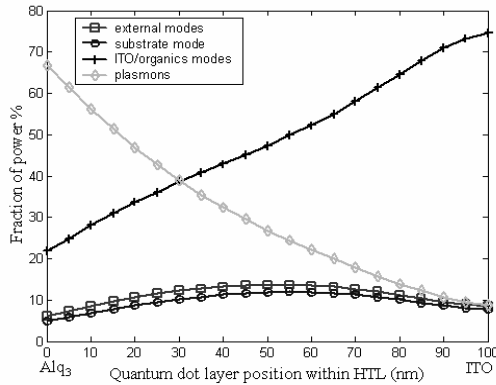


Figure 12. The fraction of the emitted power coupled into the external, substrate waveguided, ITO/organic modes and surface plasmon waveguided modes as a function of Quantum dot layer position in the HTL layer (nm).

investigated the effect of successively moving the position of the emitting center (QD) within the HTL layer on the fraction of the emitted power coupled into different optical modes. Figure 12 shows the fraction of the emitted power coupled into external, substrate waveguided, ITO/organic waveguided and surface plasmon waveguided modes as a function of emitting center (QD) position within the HTL layer. Clearly, the surface plasmon waveguided modes decrease when the emitting center is moving away from the cathode while ITO/organic waveguided mode increases. The calculation for this device shows that the maximum direct external emission occurs at ~ 50 nm distance from $\text{Alq}_3/\alpha\text{-NPD}$ interface. The calculated outcoupling efficiency for this maximum is 13.7090%.

In the following paragraphs, we will use the Green's function model to investigate the emission intensity of IR QD-LED by varying ETL and HTL thicknesses. We have studied the emission intensity of a series of structures with constant emission layer and HTL thicknesses and systematically increasing ETL thickness between 20 and 160 nm. Figure 13 shows the calculated emission intensity as a function of various Alq_3 layer thicknesses. Obviously, the emission intensity is linearly increased to a certain thickness of the ETL (~ 120 nm), in a good agreement with the previously reported experimental results for QD-LEDs [37]). And with further increasing the ETL layer thickness the emission intensity starts to decrease. In addition, the emission peak maximum starts to shift to lower energy. We ascribe this behavior to

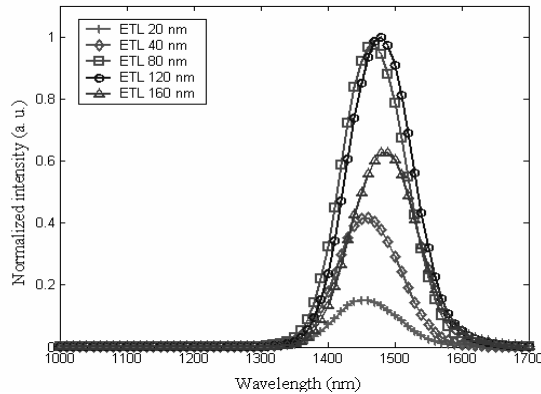


Figure 13. Calculated emission spectra of IR QD-LEDs with different ETL thicknesses.

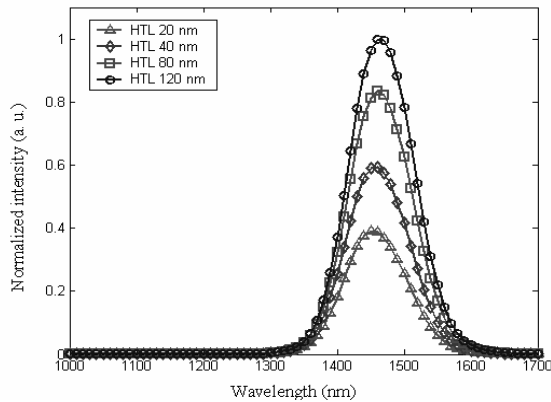


Figure 14. Calculated EL spectra of IR QD-LEDs with different HTL thicknesses.

the interference effects between the emitted wave and the reflected wave from the cathode.

We have also studied the emission intensity of a series of structures with constant thicknesses of emission layer and ELT and systematically increasing HTL thickness between 20 and 120 nm. Figure 14 shows the calculated emission spectra as a function of different thicknesses of the HTL layer (α -BPD). It is clear that the emission intensity increases with increasing the HTL layer thickness. This result is attributed to a gradually decreasing the totally resultant attenuation

of the waveguided modes.

Finally, it should be noted that the present simulation of IR QD-LEDs considers only the optimization of optical performance through the layers geometry of the device. The layer geometry of the device not only affects the optical characteristic but also affects the electrical characteristic. So, for excellent optimization we should simulate both of the optical and electrical characteristics in a parallel way, and this will be the subject of a future work.

4. CONCLUSION

We have studied the optical characteristics of QD-LED in IR region based on the Green's function method with the aim of increasing its outcoupling efficiency. We investigate the outcoupling efficiency, angular emission profile, and the radiation characteristics of IR QD-LED as a function of the thickness of the constituent layers of the device and the position of the emitting center (QD). It has been found that all these parameters affect the outcoupling efficiency of the whole device. Also, we find that the HTL and ETL thicknesses are playing an important role in the outcoupling efficiency of the device. The outcoupling efficiency improves more than five times by optimization through the geometry of the device. Finally, for excellent optimization we should simulate both of the optical and electrical characteristics in a parallel way.

REFERENCES

1. Konstantatos, G., C. Huang, L. Levina, Z. Lu, and E. H. Sargent, "Efficient infrared electroluminescent devices using solution-processed colloidal quantum dots," *Advanced Functional Materials*, Vol. 15, No. 11, 1865–1869, 2005.
2. Stok, A. and E. H. Sargent, "Lighting the local area: Optical code-division multiple access and quality of service provisioning," *IEEE Network*, Vol. 14, No. 6, 42–46, 2000.
3. Steckel, J. S., S. Coe-Sullivan, V. Bulovic, and M. G. Bawendi, "1.3 μm to 1.55 μm tunable electroluminescence from PbSe quantum dots embedded within an organic device," *Advanced Materials*, Vol. 15, No. 21, 1862–1866, 2003.
4. Tessler, N., V. Medvedev, M. Kazes, S. Kan, and U. Banin, "Efficient near-infrared polymer nanocrystal light-emitting diodes," *Science*, Vol. 295, No. 5559, 1506–1508, 2002.

5. Bakueva, L. and S. Musikhin, "Size-tunable infrared (1000–1600 nm) electroluminescence from PbS quantum-dot nanocrystals in a semiconducting polymer," *Appl. Phys. Lett.*, Vol. 82, No. 17, 2895–2897, 2003.
6. McDonald, S. A., P. W. Cyr, L. Levina, and E. H. Sargent, "Photoconductivity from PbS-nanocrystal/semiconducting polymer composites for solution-processible, quantum-size tunable infrared photodetectors," *Appl. Phys. Lett.*, Vol. 85, No. 11, 2089–2091, 2004.
7. Liu, H. C., M. Gao, J. McCaffrey, Z. R. Wasilewski, and S. Fafard, "Quantum dot infrared photodetectors," *Appl. Phys. Lett.*, Vol. 78, No. 1, 79–81, 2001.
8. Böberl, M., M. V. Kovalenko, G. Pillwein, G. Brunthaler, and W. Heiss, "Quantum dot nanocolumn photodetectors for light detection in the infrared," *Appl. Phys. Lett.*, Vol. 92, No. 26, 261113, 2008.
9. McDonald, S. A., G. Konstantatos, S. G. Zhang, P. W. Cyr, E. J. D. Klem, L. Levina, and E. H. Sargent, "Solution-processed PbS quantum dot infrared photodetectors and photovoltaics," *Nature Materials*, Vol. 4, 138–142, 2005.
10. Klem, E. J. D., L. Levina, and E. H. Sargent, "PbS quantum dot electroabsorption modulation across the extended communications band 1200–1700 nm," *Appl. Phys. Lett.*, Vol. 87, 053101, 2005.
11. Huynh, W. U., J. J. Dittmer, and A. P. Alivisatos, "Hybrid nanorod-polymer solar cells," *Science*, Vol. 295, No. 5564, 2425–2427, 2002.
12. Klimov, V. I., A. A. Mikhailovsky, S. Xu, A. Malko, J. A. Hollingsworth, C. A. Leatherdale, H.-J. Eisler, and M. G. Bawendi, "Optical gain and stimulated emission in nanocrystal quantum dots," *Science*, Vol. 290, No. 5490, 314–317, 2000.
13. Schaller, R. D., M. A. Petruska, and V. I. Klimov, "Tunable near-infrared optical gain and amplified spontaneous emission using PbSe nanocrystals," *J. Phys. Chem. B*, Vol. 107, No. 50, 13765–13768, 2003.
14. Lin, Y.-M. and M. S. Dresselhaus, "Thermoelectric properties of superlattice nanowires," *Physical Review B*, Vol. 68, No. 7, 075304, 2003.
15. Gaponik, N., I. L. Radtchenko, M. R. Gerstenberger, Y. A. Fedutik, G. B. Sukhorukov, and A. L. Rogach, "Labeling of biocompatible polymer microcapsules with near-infrared emitting nanocrystals," *Appl. Phys. Lett.*, Vol. 85, No. 11, 2089–2091, 2004.

- tals," *Nano Letters*, Vol. 3, No. 3, 369–372, 2003.
16. Bourdakos, K. N., D. M. N. M. Dissanayake, T. Lutz, S. R. P. Silva, and R. J. Curry, "Highly efficient near-infrared hybrid organic-inorganic nanocrystal electroluminescence device," *Appl. Phys. Lett.*, Vol. 92, No. 15, 153311, 2008.
 17. Zhao, J. L., J. A. Bardecker, A. M. Munro, M. S. Liu, Y. H. Niu, I.-K. Ding, J. D. Luo, B. Q. Chen, A. K.-Y. Jen, and D. S. Ginger, "Efficient CdSe/CdS quantum dot light-emitting diodes using a thermally polymerized hole transport layer," *Nano Letters*, Vol. 6, No. 3, 463–467, 2006.
 18. Lu, M.-H. and J. C. Sturm, "External coupling efficiency in planar organic light-emitting devices," *Appl. Phys. Lett.*, Vol. 78, No. 13, 1927–1929, 2001.
 19. Du, H., C. Chen, R. Krishnan, T. D. Krauss, J. M. Harbold, F. W. Wise, M. G. Thomas, and J. Silcox, "Optical properties of colloidal PbSe nanocrystals," *Nano Letters*, Vol. 2, No. 11, 1321–1324, 2002.
 20. Bakueva, L., G. Konstantatos, L. Levina, S. Musikhin, and E. H. Sargent, "Luminescence from processible quantum dot-polymer light emitters 1100–1600 nm: Tailoring spectral width and shape," *Appl. Phys. Lett.*, Vol. 84, No. 18, 3459–3461, 2004.
 21. Overhof, H. and U. Rossler, "Electronic structure of PbS, PbSe, and PbTe," *Phys. Stat. Sol.*, Vol. 37, No. 2, 691–698, 2006.
 22. Chang, T.-W. F., A. Maria, P. W. Cyr, V. Sukhovatkin, L. Levina, and E. H. Sargent, "High near-infrared photoluminescence quantum efficiency from PbS nanocrystals in polymer films," *Synthetic Metals*, Vol. 148, No. 3, 257–261, 2005.
 23. Wehrenberg, B. L., C. Wang, and P. Guyot-Sionnest, "Interband and intraband optical studies of PbSe colloidal quantum dots," *J. Phys. Chem. B*, Vol. 106, No. 41, 10634–10640, 2002.
 24. Kim, K.-H., J.-H. Shin, N.-M. Park, C. Huh, T.-Y. Kim, K.-S. Cho, J. C. Hong, and G. Y. Sung, "Enhancement of light extraction from a silicon quantum dot light-emitting diode containing a rugged surface pattern," *Appl. Phys. Lett.*, Vol. 89, No. 19, 191120, 2006.
 25. Saleh, B. E. A. and M. C. Teich, *Fundamentals of Photonics*, Wiley, New York, 1991.
 26. Chance, R. R., A. Prock, and R. Silbey, "Molecular fluorescence and energy transfer near metal interfaces," *Advances in Chemical Physics*, S. A. R. I. Prigogine (ed.), 1–65, Wiley, 1978.
 27. Celebi, K., T. D. Heidel, and M. A. Baldo, "Simplified calculation

- of dipole energy transport in a multilayer stack using dyadic Green's functions," *Optics Express*, Vol. 15, No. 4, 1762–1772, 2007.
28. Hartman, R. L., S. M. Cohen, and P. T. Leung, "A note on the green dyadic calculation of the decay rates for admolecules at multiple planar interfaces," *J. Chem. Phys.*, Vol. 110, No. 4, 2189–2194, 1999.
 29. Li, L.-W., P.-S. Kooi, M.-S. Leong, and T.-S. Yeo, "Electromagnetic dyadic Green's function in spherically multilayered media," *IEEE Trans. on Microwave Theory and Techniques*, Vol. 42, No. 12, 2302–2310, 1994.
 30. Lee, C.-C., M.-Y. Chang, Y.-D. Jong, T.-W. Huang, C.-S. Chu, and Y. Chang, "Numerical simulation of electrical and optical characteristics of multilayer organic light-emitting devices," *Jpn. J. Appl. Phys.*, Vol. 43, No. 11A, 7560–7565, 2004.
 31. Himcinschi, C., N. Meyer, S. Hartmann, M. Gersdorff, M. Friedrich, H.-H. Johannes, W. Kowalsky, M. Schwambers, G. Strauch, M. Heuken, D. R. T. Zahn, "Spectroscopic ellipsometric characterization of organic films obtained via organic vapor phase deposition," *Appl. Phys. A*, Vol. 80, No. 3, 551–555, 2005.
 32. *Handbook of Optical Constants of Solids*, E. D. Palik (ed.), Academic, New York, 1985.
 33. Seth Coe, W.-K. W., M. Bawendi, and V. Bulović, "Electroluminescence from single monolayers of nanocrystals in molecular organic devices," *Nature Materials*, Vol. 420, 800–803, 2002.
 34. Patel, N. K., S. Cinà, and J. H. Burroughes, "High-efficiency organic light-emitting diodes," *IEEE J. Select. Topics Quantum Electron.*, Vol. 8, No. 2, 346–361, 2002.
 35. Lu, M.-H. and J. C. Sturm, "Optimization of external coupling and light emission in organic light-emitting devices: Modeling and experiment," *J. Appl. Phys.*, Vol. 91, No. 2, 595–604, 2002.
 36. Kim, H., C. M. Gilmore, A. Piqué, J. S. Horwitz, H. Mattoussi, H. Murata, Z. H. Kafafi, and D. B. Chrisey, "Electrical, optical, and structural properties of indium-tin-oxide thin films for organic light-emitting devices," *J. Appl. Phys.*, Vol. 86, No. 11, 6451–6461, 1999.
 37. Sun, Q. J., Y. A. Wang, L. S. Li, D. Y. Wang, T. Zhu, J. Xu, C. H. Yang, and Y. F. Li, "Multicoloured light-emitting diodes based on quantum dots," *Nature Photonics*, Vol. 1, 717–722, 2007.